Physics of Fluids ARTICLE scitation.org/journal/phf

Data-driven global stability of vertical planar liquid jets by dynamic mode decomposition on random perturbations

Cite as: Phys. Fluids **34**, 122101 (2022); doi: 10.1063/5.0123550
Submitted: 31 August 2022 · Accepted: 4 November 2022 ·
Published Online: 1 December 2022

View Online Export Citation CrossMark

Antonio Colanera,[a] Alessandro Della Pia, and Matteo Chiatto

AFFILIATIONS

Department of Industrial Engineering, Aerospace Sector, Università degli Studi di Napoli "Federico II", Naples 80125, Italy

[a]Author to whom correspondence should be addressed: antonio.colanera@unina.it

ABSTRACT

A data-driven approach to estimate the global spectrum of gravitational planar liquid jets (sheet or curtain flows) is presented in this work. The investigation is carried out by means of two-dimensional numerical simulations performed through the solver BASILISK, based on the one-fluid formulation and the volume-of-fluid approach. The dynamic mode decomposition technique is applied to extract the underlying linear operator, considering random perturbations of the base flow. The effectiveness of this procedure is first evaluated comparing results with those of a simplified one-dimensional curtain model in terms of spectrum and eigenfunctions. The methodology is then applied to a two-dimensional configuration obtaining the BiGlobal spectra for both supercritical (Weber number $We > 1$) and subcritical ($We < 1$) regimes. Results highlight that in supercritical regime, the spectrum presents three branches: the upper and lower ones exhibit a purely sinuous behavior with frequencies quite close to those predicted by the one-dimensional model; the middle branch presents a predominant varicose component, increasing with the frequency. The subcritical spectrum, instead, shows that the first two less stable eigenvalues, sorted by increasing frequency, exhibit, respectively, a sinuous and a varicose behavior, while their growth rate is almost the same. As expected, the subcritical regime does not reveal the slow branch. The effect of the density ratio, r_ρ, between the two phases is investigated, revealing that the flow system is unstable for $r_\rho > 0.05$. Topological inspections of the leading modes in this unstable configuration show that the predominance of a varicose behavior is related to the rupture of the curtain.

Published under an exclusive license by AIP Publishing. https://doi.org/10.1063/5.0123550

I. INTRODUCTION

Vertical planar gravitational liquid jets (sheet or curtain flows) are an interesting industrial class of flows, whose modeling has been investigated since the middle of the last century. Typical applications are coating layer deposition[1] and paper production.[2] The ability to control and eventually suppress undesired oscillations (or non-uniformities) in steady configurations is fundamental for the final quality of an industrial process. Vertical curtain flows are also related to the nappe configuration, that is, the flow of waterfalls generated by the overflow of water over long crests of dams or weirs.[3–5] One of the major drawbacks of these flows is related to the onset of self-sustained oscillations, which can lead to significant noise levels and structural damages.

Due to gravitational effects, the flow field is not parallel and the determination of the oscillation frequencies of the liquid jet involves a global problem essentially governed by the Weber number. The global stability analysis has been until now theoretically carried out by using a linear one-dimensional (1D) model[6,7] and taking advantage from an energy budget approach.[8] A recent application of data-driven techniques to liquid jets has been presented by Arote *et al.*[9] who focused on the effect of the Reynolds number on the topology of the flow; moreover,[10,11] explored the effect of a continuous harmonic perturbation enforced at the inlet section on the main coherent structures of the unsteady field and the related temporal frequencies. Recently, Schmidt and Oberleithner[12] studied the stability of planar liquid jets, harmonically forcing the transversal velocity at the inlet section without gravitational effects.

Modal decomposition techniques represent a powerful tool to gain further physical insights on fluid dynamics problems through the identification and the analysis (in terms of spatiotemporal evolution) of the main coherent structures of the flow.[13] The recent increase in computing power encouraged the development of many data-driven analysis tools.[14,15] In particular, the rediscovery of Koopman spectral analysis by Mezic[16] and Rowley *et al.*[17] traced the road map for the formulation of the dynamic mode decomposition (DMD) by Schmid[18] and Tu *et al.*[19] DMD generates the best linear fit data-driven

Published under an exclusive license by AIP Publishing

model and provides structures ranked according to the dynamics of the system. Its application field is quite wide including the analysis of fluid flows in several configurations,[20] face recognition,[21] and neuroscience.[22]

One classical way of examining fluid flows is by linearizing the governing equations, and studying the mathematical evolution of disturbances (of small-amplitude) superposed on a base flow. This approach provides the eigenvalue spectrum of the system, revealing the emergence of the flow unsteadiness and thus allowing the prediction of flow-field dominant frequencies.[23–26] However, spectral information of the system can be also obtained by means of the DMD technique that can be conveniently applied instead of the linearization procedure as shown in Ferrer *et al.*[27] and Ranjan *et al.*[28]

In this case, the DMD provides the linear relationship between a generic snapshot and the subsequent one, considering random perturbations of the base flow. Other very recent applications involve data-driven resolvent analysis[29] and optimally time-dependent modes.[30] This approach avoids the linearization process of the governing equations, together with the related numerical and theoretical complexity.

The aim of this work is to analyze the global spectra of viscous gravitational two-dimensional (2D) liquid sheets by applying the DMD technique on randomly perturbed base flows. The DMD is used to estimate the linearized evolution operator and to extract the main spatial structures, together with information on the system dynamics. The flow fields have been obtained by means of numerical simulations performed with the two-phase code BASILISK.[31] To the authors' best knowledge, this is the first time that the DMD technique is applied to a multiphase flow field for this purpose; the analysis of the liquid sheet BiGlobal spectrum represents a novelty as well.

The paper is organized as follows: Sec. II contains a brief introduction of the physical layout and the governing equations. Section III is devoted to the methodology, focusing on the base flow perturbation and the DMD algorithm for the estimation of the underlying linear operator, with related eigenspectra/eigenfunctions. Section IV reports the results first for the 1D model and then for the 2D configurations.

II. PHYSICAL AND COMPUTATIONAL LAYOUT

The flow here considered is a gravitational viscous liquid jet interacting on both sides with an unconfined gaseous ambient. Panel (a) of Fig. 1 contains a sketch of the system, together with the reference frame: its origin is coincident with the center of the inlet flow section (whose width is denoted by H), and the x axis is directed along the streamwise direction, while the y axis is across the width of the sheet. Red lines represent the symmetric unperturbed flow, corresponding to the Torricellian solution whose thickness ($\bar{h}(x)$) is described by the law

$$\frac{\bar{h}(x)}{H} = \left(1 + \frac{2g}{U^2}x\right)^{-1/2}, \tag{1}$$

where U is the mean axial velocity at the inlet section and g is the gravity acceleration. Black lines, instead, correspond to the instantaneous left and right interface locations, and are denoted with $y^-(x,t)$ and $y^+(x,t)$, respectively. Accordingly, the centerline deflection, $l(x,\ t)$, and the sheet thickness, $h(x,\ t)$, are computed as

$$\begin{bmatrix} l(x,t) \\ h(x,t) \end{bmatrix} = \begin{bmatrix} 1/2 & 1/2 \\ 1 & -1 \end{bmatrix} \begin{bmatrix} y^+(x,t) \\ y^-(x,t) \end{bmatrix}. \tag{2}$$

The numerical investigation has been carried out by means of the BASILISK open-source code.[31] It is based on the single-phase formulation[32] and the volume-of-fluid (VOF) approach[33] in which the two-phase flow is considered as a one-fluid flow with the introduction of the volume fraction, C. The volume fraction is a field variable equal to 1 in the inner phase and 0 in the ambient phase; the interface corresponds to $C = 0.5$. In this framework, density, ρ, and viscosity, μ, are modeled as

$$\rho = \rho_a + (\rho_l - \rho_a)C, \tag{3a}$$

$$\mu = \mu_a + (\mu_l - \mu_a)C, \tag{3b}$$

where pedici a and l refer to the ambient and the liquid phase, respectively. The main physical quantities, defining the base case involved in the problem, are listed in Table I.

The momentum equations and the divergence-free condition, in the index notation, are

$$\rho\left(\frac{\partial u_i}{\partial t} + u_j\frac{\partial u_i}{\partial x_j}\right) = -\frac{\partial p}{\partial x_i} + \frac{\partial}{\partial x_j}\left[\mu\left(\frac{\partial u_i}{\partial x_j} + \frac{\partial u_j}{\partial x_i}\right)\right] + \sigma\kappa n_i\delta_S, \tag{4a}$$

$$\frac{\partial u_i}{\partial x_i} = 0, \tag{4b}$$

in which the surface tension effect is modeled as an impulsive force located at the interface, namely, $\sigma\kappa n_i\delta_S$, where σ is the surface tension, κ the interface curvature, n_i the ith component of the normal versor $\mathbf{n}$, and δ_S a Dirac function on the interface. Following Popinet,[31] $\mathbf{n}$ and κ are computed as: $\mathbf{n} = \nabla\tilde{C}/|\nabla\tilde{C}|$ and $\kappa = \nabla\cdot\mathbf{n}$, where $\tilde{C}$ is a smoothed (i.e., diffused) version of the sharp volume fraction field. The effects of the gravitational field are contained in the pressure term p. For the closure problem,[33] C has to satisfy the advection equation:

$$\frac{\partial C}{\partial t} + \frac{\partial C u_i}{\partial x_i} = 0. \tag{5}$$

The computational domain is a square with sides equal to $L = 50H$ ($\varepsilon = H/L = 0.02$); its representation is reported in panel (b) of Fig. 1. The boundary conditions for the axial (u) and transversal (v) velocity components at the inlet section ($-0.5 < y/H < 0.5$ and $x/L = 0$) are as follows:

$$u = \frac{3}{2}U\left[1 - \left(\frac{2y}{H}\right)^2\right], \quad v = 0, \quad C = 1, \tag{6}$$

corresponding to a fully developed parabolic velocity profile for u.

At the exit section, standard outflow conditions for u, v, and C and the differential pressure p are imposed

$$\frac{\partial u}{\partial x} = 0, \quad \frac{\partial v}{\partial x} = 0, \quad \frac{\partial C}{\partial x} = 0, \quad p = 0. \tag{7}$$

Homogeneous Neumann boundary conditions are imposed for all variables at the right and left sides. The computational grid employed is a quad-tree adaptive grid, retaining its maximum level of refinement in a rectangular region containing the liquid sheet ($0 < x/L < 1, -0.5 < y/H < 0.5$). The minimum dimensionless cell edge length is $\Delta x/H = 0.0488$ corresponding to 20 cells within H. This choice has been supported by a grid convergence analysis, as

Published under an exclusive license by AIP Publishing

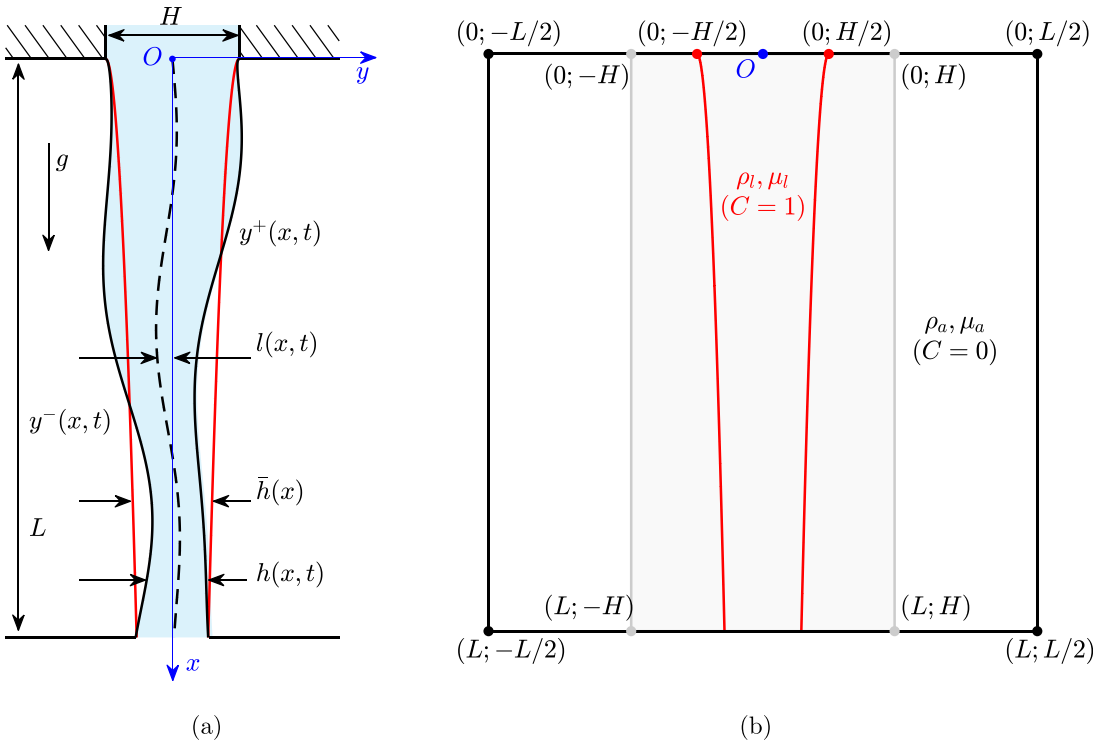

FIG. 1. Sketch of physical (a) and computational (b) domains. The red lines represent the steady (or mean) interface locations corresponding to the Torricellian shape.

done in the work by Della Pia *et al.*,[6] based on the ratio between the outlet sheet thickness and the inlet one (not reported herein). The gray patch $(0 < x/L < 1, -1 < y/H < 1)$ highlights the region considered for the modal analysis. Note that the axes have been scaled with different variables. The simulation time step is evaluated at each iteration as follows:

$$\Delta t_s = \min\left(\frac{0.5\Delta x}{u}, \sqrt{\rho_l \frac{1+r_\rho}{2}\frac{\Delta x^3}{\pi\sigma}}\right), \tag{8}$$

in which ρ_l is the density of the liquid phase, r_ρ is the ratio between ambient and liquid phase densities ρ_a/ρ_l, and σ is the surface tension.

TABLE I. Dimensional physical quantities involved in the problem, corresponding to the base case.

Name	Variable	Values	Units
Inlet liquid mean velocity	U	0.49	m s^{-1}
Inlet sheet thickness	H	1.5×10^{-3}	m
Sheet length	L	75×10^{-3}	m
Surface tension coefficient	σ	72.5×10^{-3}	N m^{-1}
Gravity acceleration	g	9.81	m s^{-2}
Ambient density	ρ_a	9.97	kg m^{-3}
Liquid density	ρ_l	997	kg m^{-3}
Ambient viscosity	μ_a	1.84×10^{-5}	kg m^{-1} s^{-1}
Liquid viscosity	μ_l	8.90×10^{-4}	kg m^{-1} s^{-1}

The behavior of the flow is completely characterized through a few dimensionless parameters, as observed by Della Pia *et al.*[6] In particular, relevant variables are related both to geometrical features, such as the sheet slenderness ratio $\varepsilon = H/L$, and to physical quantities as the Reynolds number $Re = \rho_l UH/(2\mu_l)$, the Froude number $Fr = U^2/(gL)$, the Weber number $We = \rho_l U^2 H/(2\sigma)$, and the density ratio $r_\rho = \rho_a/\rho_l$. Table II contains the values of the main parameters for the configurations here analyzed; we note that the bold values refer to the base case.

III. DATA-DRIVEN GLOBAL STABILITY ANALYSIS

The global stability analysis focuses on the temporal and spatial evolution of small-amplitude perturbations superimposed upon a base flow. In the framework of two-phase flows, it is convenient to define a state vector $\mathbf{q}$ by stacking the velocity components and the volume fraction at every time instance. With this assumption, the governing

TABLE II. Dimensionless parameters involved in the numerical analysis. Bold values refer to the base case.

Name	Definition	Values
Gas-to-liquid density ratio	$r_\rho = \rho_a/\rho_l$	0.005, **0.01**, 0.05
Sheet slenderness ratio	$\varepsilon = H/L$	**0.02**
Reynolds number	$Re = \rho_l UH/(2\mu_l)$	**413**
Froude number	$Fr = U^2/(gL)$	**0.329**
Weber number	$We = \rho_l U^2 H/(2\sigma)$	0.75, 1.5, **2.5**, 3.5

Published under an exclusive license by AIP Publishing

equations (4) and (5) can be recast in the form of a classic first-order dynamical system,

$$\dot{\mathbf{q}} = f(\mathbf{q}), \tag{9}$$

with f being a non-linear operator depending on $\mathbf{q}$.

From a practical point of view, the analysis is carried out through the decomposition of $\mathbf{q}$ in the sum of a base flow $\bar{\mathbf{q}}$ and the fluctuations $\mathbf{q}'$, such that $\mathbf{q} = \bar{\mathbf{q}} + \mathbf{q}'$; in this way, it is possible to obtain the linearized form of Eq. (9)

$$\dot{\mathbf{q}}' = \mathbf{L}_{\bar{\mathbf{q}}}\mathbf{q}', \tag{10}$$

with $\mathbf{L}_{\bar{\mathbf{q}}}$ being the Jacobian operator evaluated at the base flow.

The computation of $\mathbf{L}_{\bar{\mathbf{q}}}$ is numerically prohibitive. Theofilis[34] and Bagheri *et al.*,[35] in the hypothesis of small perturbations, showed that its evaluation can be simplified when based on instantaneous fields of $\mathbf{q}'$ (snapshots), obtained by a high-order solver (in present case the BASILISK). Moreover, following Gomez *et al.*[36] a proper set of snapshots is constructed through the Fréchet derivative:

$$\dot{\mathbf{q}}' = \mathbf{L}_{\bar{\mathbf{q}}}\mathbf{q}' = \left.\frac{\partial f(\mathbf{q})}{\partial \mathbf{q}}\right|_{\bar{\mathbf{q}}} \mathbf{q}' \approx f(\bar{\mathbf{q}}+\mathbf{q}') - f(\bar{\mathbf{q}}), \tag{11}$$

which, when integrated from a generic time instance $t = t_n$ to the subsequent one $t = t_n + \Delta t$, leads to

$$\mathbf{q}'_{n+1} = e^{\mathbf{L}_{\bar{\mathbf{q}}}\Delta t}\mathbf{q}'_n = \mathbf{A}\mathbf{q}'_n \approx \int_{t_n}^{t_n+\Delta t} f(\bar{\mathbf{q}}+\mathbf{q}')dt - \int_{t_n}^{t_n+\Delta t} f(\bar{\mathbf{q}})dt. \tag{12}$$

The inspection of the previous equation highlights the linear relationship between two subsequent snapshots $\mathbf{q}'_n$ and $\mathbf{q}'_{n+1}$ through the matrix $\mathbf{A}$; we note that $\mathbf{A}\mathbf{q}'_n$ approximates the difference between the variation of the perturbed field and that of the base flow.

The base flow $\bar{\mathbf{q}}$ has been assumed coincident with the flow field after an evolving time $t_0 = 6t_r$, where t_r is the reference time $t_r = L/U$. The perturbed field has been obtained by adding a purely random perturbation to the whole flow field at $t = t_0$. In particular, this perturbation is modeled as white noise, with an amplitude of 1% of U for the velocity components (u and v) and 0.01 for the volume of fraction in the interface region.

The matrix $\mathbf{A}$ has been obtained by means of the DMD technique,[28] which decomposes time-resolved data into modes, each of one with its own frequency and growth rate. Considering a standard DMD algorithm,[19] it is convenient to define a physically meaningful norm for $\mathbf{q}'$ related to the fluctuations energy of the velocity components and of the volume fraction. In particular, the norm is $\|\mathbf{q}'\|^2_{\mathbf{P}} = \mathbf{q}'^*\mathbf{P}\mathbf{q}'$, where $(\cdot)^*$ denotes the conjugate transpose operator and $\mathbf{P}$ represents a weight matrix whose elements have been computed according to the work of Chu[37] providing the following energy norm:

$$E = \int_\Omega \left[\bar{\rho}(u'^2 + v'^2) + (\bar{u}^2 + \bar{v}^2)\frac{\Delta\rho^2}{\bar{\rho}}C'^2\right] d\Omega, \tag{13}$$

in which Ω is the computational domain. In this way, $\mathbf{P}$ takes into account the integration quadratures and appropriate scaling of heterogeneous variables of the problem. Finally, a Cholesky decomposition $\mathbf{P} = \mathbf{F}^*\mathbf{F}$ has been computed to obtain $E = \|\mathbf{q}'\|^2_{\mathbf{P}} = \mathbf{q}'^*\mathbf{F}^*\mathbf{F}\mathbf{q}' = \|\mathbf{F}\mathbf{q}'\|^2_2$.

The DMD algorithm considers the snapshots ($\mathbf{F}\mathbf{q}'_k$) collected as columns in the matrices $\mathbf{Q}_1$ and $\mathbf{Q}_2$

$$\mathbf{Q}_1 = \mathbf{F}\begin{bmatrix} | & & | & & | \\ \mathbf{q}'_1 & \cdots & \mathbf{q}'_k & \cdots & \mathbf{q}'_M \\ | & & | & & | \end{bmatrix},$$
$$\mathbf{Q}_2 = \mathbf{F}\begin{bmatrix} | & & | & & | \\ \mathbf{q}'_2 & \cdots & \mathbf{q}'_{k+1} & \cdots & \mathbf{q}'_{M+1} \\ | & & | & & | \end{bmatrix}, \quad \mathbf{Q}_1, \mathbf{Q}_2 \in \mathbb{R}^{N\times M}, \tag{14}$$

where N is the cardinality of the state vector $\mathbf{q}'$, and M the number of snapshots. In this view, the linear operator approximates the temporal dynamics of the data such that

$$\mathbf{Q}_2 \approx \mathbf{\Theta}\mathbf{Q}_1. \tag{15}$$

It is worth noting that the matrix $\mathbf{\Theta}$ is related to the matrix $\mathbf{A}$ by $\mathbf{\Theta} = \mathbf{F}\mathbf{A}\mathbf{F}^{-1}$; it shares the same eigenvalues of $\mathbf{A}$ and has eigenvectors scaled by $\mathbf{F}$. Moreover, snapshots collected within the matrices $\mathbf{Q}_1$ and $\mathbf{Q}_2$ can also refer to several simulations with different random initializations.[29] The following analysis considers 200 simulations each one of 200 snapshots, with $\Delta t = 10\,\Delta t_s \approx 0.003\,t_r$.

The leading coherent structures (namely, the DMD modes) are evaluated through the SVD decomposition of $\mathbf{Q}_1$, according to which $\mathbf{Q}_1 = \mathbf{U}\mathbf{\Sigma}\mathbf{V}^*$. In this way, Eq. (15) becomes $\mathbf{\Theta} = \mathbf{Q}_2\mathbf{V}\mathbf{\Sigma}^{-1}\mathbf{U}^*$, which generally requires a large computational cost. To mitigate this effort, it is convenient to introduce the matrix $\tilde{\mathbf{\Theta}} = \mathbf{U}^*\mathbf{Q}_2\mathbf{V}\mathbf{\Sigma}^{-1}$ that shares the same non-zero eigenvalues of $\mathbf{\Theta}$ (and of $\mathbf{A}$), but has a lower dimension and thus requires a reduced numerical cost. Finally, the DMD modes $\mathbf{\Phi}$ are retrieved as $\mathbf{\Phi} = \mathbf{Q}_2\mathbf{V}\mathbf{\Sigma}^{-1}\mathbf{W}$, with $\mathbf{W}$ being the matrix of eigenvectors of $\tilde{\mathbf{\Theta}}$.

The dimensionless spectrum of the underlying linear operator $\mathbf{L}_{\bar{\mathbf{q}}}$ is computed by

$$\lambda_k = \lambda_r + \lambda_i\, i = \frac{\log(\mu_k)}{\Delta t}2\pi t_r, \tag{16}$$

where μ_k is the kth eigenvalue of $\tilde{\mathbf{\Theta}}$, λ_r is the dimensionless growth rate, and λ_i is the dimensionless frequency. Note that throughout this work relevant eigenvalues are represented with two decimal digits only.

The convergence and the saturation of the DMD algorithm are evaluated by means of the L_2 norm of the residual $\mathbf{r}$. Indeed, considering the qr factorization of the snapshots matrix ($\mathbf{Q}_1 = \mathbf{S}\mathbf{R}$) the residual $\mathbf{r}$ is defined as

$$\mathbf{r} = \mathbf{q}'_{M+1} - \mathbf{Q}_1\mathbf{R}^\dagger\mathbf{S}^*\mathbf{q}'_{M+1}, \tag{17}$$

in which $\mathbf{q}'_{M+1}$ is the last snapshot and $(\cdot)^\dagger$ is the pseudoinverse operator. Note that $\mathbf{r}$ is the reconstruction error field of the last snapshot $\mathbf{q}'_{M+1}$ and simply represents how well the last snapshot can be represented as a linear combination of the first M ones.

IV. RESULTS

A. 1D global analysis

The methodology illustrated in Sec. III is first tested on the simplified 1D model of the curtain flow described by Della Pia *et al.*,[6] which provides the streamwise distribution of both the sheet centerline

Published under an exclusive license by AIP Publishing

lateral displacement (ℓ_s) and the lateral velocity on the centerline (v_s) for sinuous perturbations of the jet. Results of the linear stability analysis carried out by means of the 1D model will be hereafter compared with those obtained by the application of the DMD technique to the same simplified flow data.

The dimensionless 1D model is based on the following governing equations:

$$\frac{\partial v_s}{\partial \hat{t}} - RU_s \int_0^1 \frac{\partial v_s}{\partial \hat{t}} \ln|\hat{x}-\xi| d\xi + RU_s \int_0^1 U_s \frac{\partial^2 \ell_s}{\partial \hat{t}\partial \hat{x}} \ln|\hat{x}-\xi| d\xi = -U_s \frac{\partial v_s}{\partial \hat{x}} + \frac{U_s}{We}\frac{\partial^2 \ell_s}{\partial \hat{x}^2} + \frac{\varepsilon}{2Re}\frac{\partial^2 v_s}{\partial \hat{x}^2}, \tag{18}$$

$$\frac{\partial \ell_s}{\partial \hat{t}} = v_s - U_s \frac{\partial \ell_s}{\partial \hat{x}}, \tag{19}$$

where $\hat{t} = t/t_r$ and $\hat{x} = x/L$ coupled with only homogeneous boundary conditions at the inlet section, $\ell_s(0) = 0$, $v_s(0) = 0$, being the free-outflow condition at the bottom edge self-guaranteed.[4] Equation (18) represents the momentum equation averaged along the lateral coordinate y and contains the unsteady Bernoulli-based pressure model by Kornecki *et al.*;[38] Eq. (19), instead, is the linearized kinematic boundary condition imposed at the free interfaces.[4] The parameter R takes in account the effects of the density ratio, r_ρ, and the sheet slenderness, ε, while U_s is the dimensionless axial velocity (corresponding to the free fall Torricellian base flow)

$$R = \frac{2}{\pi}\frac{1}{\varepsilon} r_\rho, \quad U_s(\hat{x}) = \sqrt{1 + 2\frac{\hat{x}}{Fr}}. \tag{20}$$

The analysis starts by considering supercritical flow conditions ($We > 1$). Note that in this one-dimensional analysis, unlike the subsequent two-dimensional one, the state vector $\mathbf{q}'$ consists of a collection of the values of ℓ_s and v_s in each streamwise location, and snapshots of the simulation are taken by integrating the system (18) and (19). Accordingly, the weight matrix is computed by considering the perturbations energy per unit length given by Olsson and Henningson[39] and Della Pia *et al.*[8]

$$E_{1D} = \frac{1}{2}\int_0^1 \left[\frac{v_s^2}{U_s} + \frac{1}{We}\left(\frac{\partial \ell_s}{\partial \hat{x}}\right)^2\right] d\hat{x}, \tag{21}$$

in which the first term, proportional to v_s^2, is related to the kinetic energy, whereas the second one, proportional to $(\frac{\partial \ell_s}{\partial \hat{x}})^2$, involves the surface tension.

Panel (a) of Fig. 2 reports the global spectrum computed with the linear stability theory (LST), together with the ones estimated through the DMD technique for several numbers of random initializations (n_s). The physical conditions are represented by the following set of parameters: $We = 2.5$, $Fr = 0.33$, $\varepsilon = 0.02$, $r_\rho = 0.01$, and $Re = 413$. The LST spectrum, as reported by Della Pia *et al.*,[6] exhibits two branches [see the zoom reported in panel (b)], with an almost constant spacing between the imaginary part of the eigenvalues, which is directly associated with the crossing time of slow (upper branch) and fast (lower branch) traveling waves.

The cases represented consider $n_s = 1$, 7, and 10. It is interesting to observe that with a few random snapshots ($n_s = 7$), the spectrum exhibits spurious unstable eigenvalues, but with a slight increase in n_s, it quickly tends to converge to the standard one (open circles) for both branches. For $n_s = 10$, a good match can be appreciated, the leading eigenvalues being properly captured both in real part (growth/decay rate) and imaginary one (frequency). Note that the convergence of the residuals comes with the convergence of the eigenvalues and the disappearance of the spurious ones. For the analyzed case, the leading dimensionless frequency (imaginary part of the leading eigenvalue) is $\lambda_i = 3.64$.

The leading eigenfunctions of displacement [φ_l, panel (a)] and lateral velocity [φ_v, panel (b)] for the cases $n_s = 7$ and 10 together with those based on the LST method are reported in Fig. 3. The DMD modes computed with $n_s = 10$ exhibit a very good match with the theoretical ones; the case with $n_s = 7$ is interesting because even if the leading modes exhibit spurious oscillations due to the randomness of the perturbations, the streamwise trend of these modes is correctly predicted.

The convergence and the saturation of the algorithm are evaluated by means of the L_2 norm of the residual, $\|\mathbf{r}\|$, which measures how much the last snapshot $\mathbf{q}'_{M+1}$ can be expressed as a linear combination of first M ones.[18] The trend of the residue is reported in Fig. 4 as a function of the number of simulations n_s. In accordance with the spectrum considered above, a rapid convergence can be observed for $n_s > 8$, for which $\|\mathbf{r}\| \approx 10^{-12}$, thus providing a sufficient accuracy to determine the spectrum and the corresponding eigenmodes.

Once the capability of the DMD algorithm in determining the eigenfunctions/eigenvalues of the underlying linear system has been proven, it is interesting to test its ability to properly represent the evolution of the system by comparing results of its integration with the theoretical ones [Eqs (18) and (19)].

Indeed, the linear operator $\mathbf{A}$ can be used to predict the behavior of the system in both free and forced configurations; to do that, the system (18) and (19) is recast in the form

$$\mathbf{M}\dot{\mathbf{q}}' = \mathbf{L}\mathbf{q}' + \mathbf{b}_1\mathbf{f} + \mathbf{b}_2\dot{\mathbf{f}}, \tag{22}$$

where $\mathbf{f}$ models the effect of an external forcing at the inlet ($\hat{x} = 0$), through non-homogeneous boundary conditions: $\mathbf{f} = [v_s(0,\hat{t}); \ell_s(0,\hat{t})]$. For discrete times, the solution reads

$$\mathbf{q}'_{n+1} = \mathbf{A}_{LST}\mathbf{q}'_n + \mathbf{B}_1\mathbf{f}_n + \mathbf{B}_2\dot{\mathbf{f}}_n, \tag{23}$$

in which $\mathbf{A}_{LST} = e^{(\mathbf{M}^{-1}\mathbf{L})\Delta t}$, $\mathbf{f}_n$, and $\dot{\mathbf{f}}_n$ are the forcing and its derivative at the nth time step, respectively; the matrices $\mathbf{B}_1$ and $\mathbf{B}_2$ are equal to

$$\mathbf{B}_1 = \int_0^{\Delta t} e^{(\mathbf{M}^{-1}\mathbf{L})(\Delta t-\tau)}\mathbf{b}_1 d\tau, \quad \mathbf{B}_2 = \int_0^{\Delta t} e^{(\mathbf{M}^{-1}\mathbf{L})(\Delta t-\tau)}\mathbf{b}_2 d\tau. \tag{24}$$

Figure 5 shows the solution obtained enforcing homogeneous conditions for ℓ_s and a harmonic forcing ($f_f = 25$ Hz) for the transverse velocity $v_s(0,\hat{t}) = \sin(2\pi t_r f_f \hat{t})$. A comparison between the integration of Eq. (23) by using $\mathbf{A}_{LST}$ and the DMD estimations of $\mathbf{A}$ is reported. Again, as n_s increases the DMD modes tend to behave strictly as the eigenfunctions of the LST model. Note that for $n_s = 7$, despite the quite noisy modes of the DMD model, an acceptable averaged representation of the centerline deflection (blue lines) is achieved.

B. 2D analysis

The methodology described above is now applied to 2D numerical simulations, providing an estimation of the BiGlobal spectrum in a

Published under an exclusive license by AIP Publishing

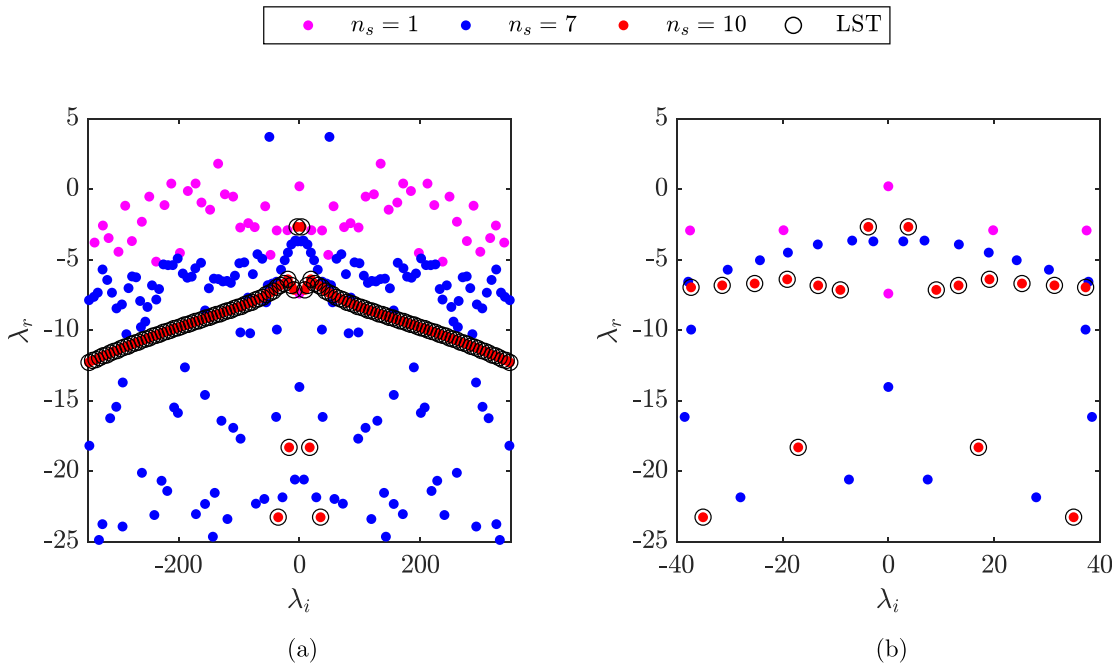

FIG. 2. Comparison between the supercritical spectrum evaluated with the linear stability analysis and various spectra computed with the DMD approach for different values of n_s. Panel (a) contains the global spectrum, and panel (b) a zoom of its inner region. $We = 2.5$, $Fr = 0.33$, $\varepsilon = 0.02$, $r_\rho = 0.01$, and $Re = 413$.

non-intrusive way, namely, without the linearization of the governing equations.

As stated before, the perturbation is imposed at the initial time in a random way (white noise) in both the velocity components and volume fraction fields. Its evolution, for the axial velocity (u') field only, can be appreciated considering the snapshots reported in Fig. 6. Panel (a) contains the white noise added to the velocity component at the initial time ($t = 0$); panels (b) and (c) show the evolution of these disturbances that, while reducing in amplitude, excite dynamics with different scales.

The study exploits the DMD technique to obtain the global spectrum; in this case, 200 simulations, corresponding to 40 000 snapshots, have been used for the analysis. The DMD spectrum of the base case has been reported in Fig. 7, together with the corresponding one of the 1D model (red circles), for a direct comparison. Here, only 400 DMD modes are reported, which retain more than the 99.9% of the POD (proper orthogonal decomposition) total energy, avoiding the introduction of spurious modes.[18]

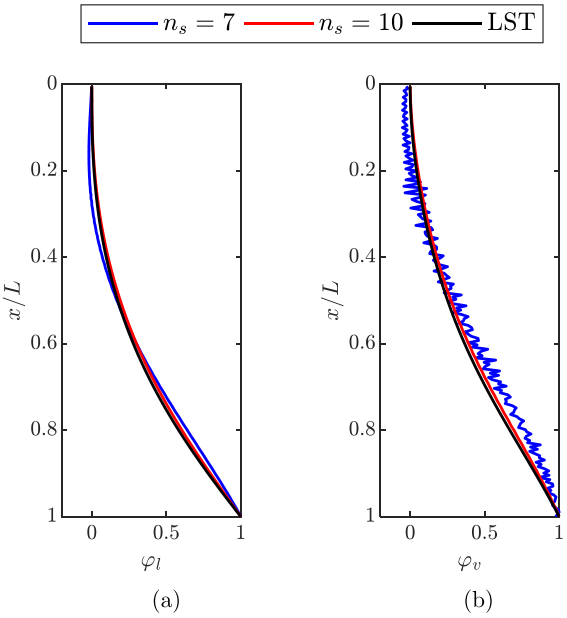

FIG. 3. Comparison between leading LST eigenfunctions and DMD modes of lateral displacement (a) and transverse velocity (b).

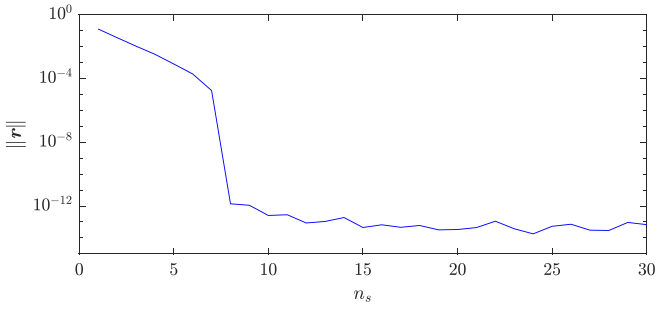

FIG. 4. Convergence of DMD algorithm. Residual value history vs number of random simulations n_s.

Published under an exclusive license by AIP Publishing

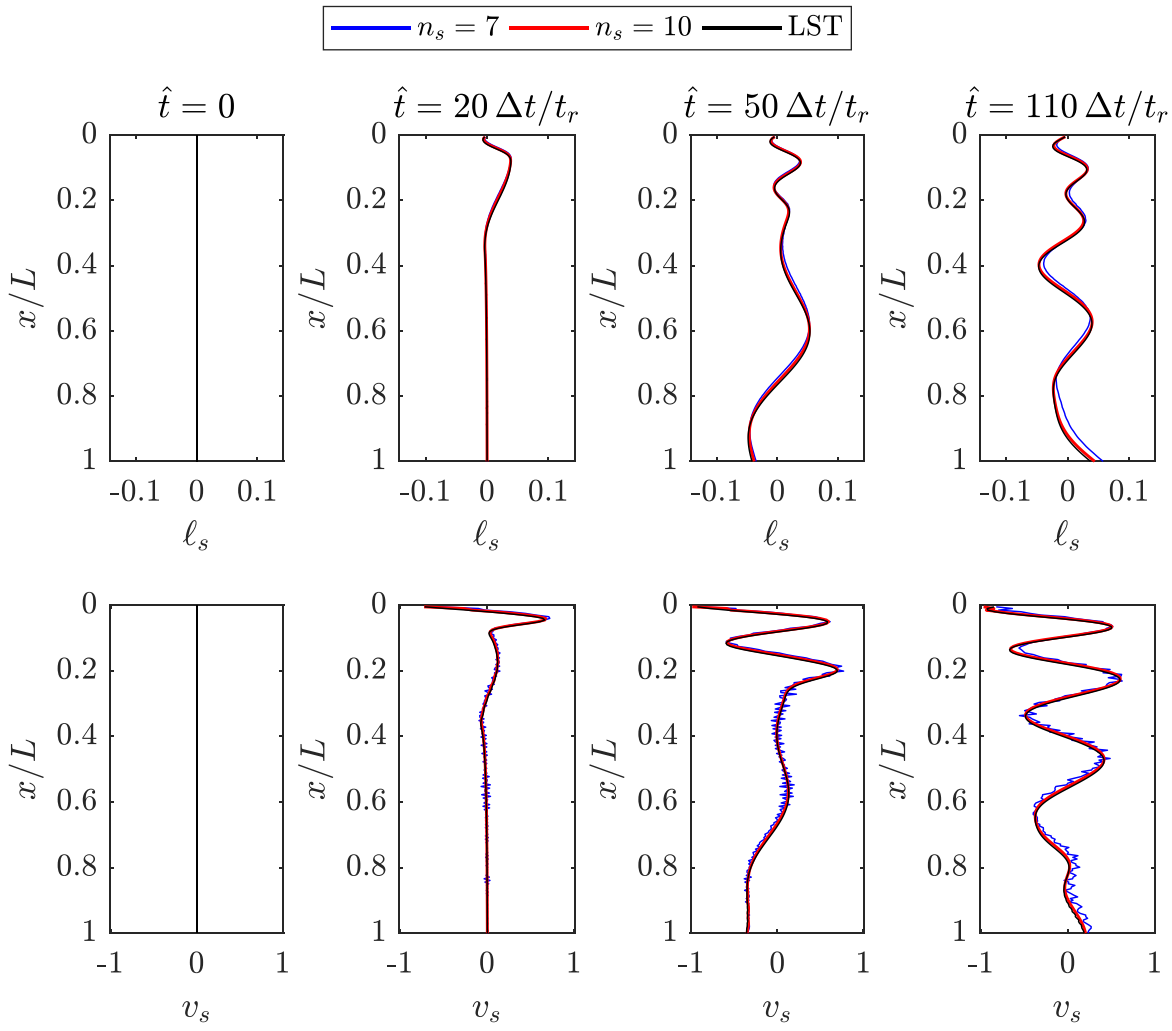

FIG. 5. Comparison between sheet centerline snapshots of the forced configuration and the same results obtained by means of the DMD approach. $We = 2.5$, $Fr = 0.33$, $\varepsilon = 0.02$, $r_\rho = 0.01$, and $Re = 413$. Sinusoidal forcing of v_s at inlet, $v_s(0, \hat{t}) = \sin(\hat{f}_f \hat{t})$ with $\hat{f}_f = 25$.

In general, the BiGlobal spectrum highlights a wider frequency content than the LST results, with a further branch in between the upper and lower branches previously found for the 1D model. The physical relevance of the middle branch will be discussed hereafter. All the eigenvalues have a negative real part due to the stable nature of the flow; the less damped eigenvalues are located at low frequencies. The leading mode, labeled A, is equal to $\lambda = -0.54 + 3.64\,\mathrm{i}$ which perfectly matches the value predicted by the low-order analysis; other interesting eigenvalues are highlighted with blue circles in the spectrum and are located on different branches: modes A and B belong to the upper branch; modes C, D, and E are on the middle one; and mode F lies on the lower branch. The corresponding values are reported in Table III.

The DMD technique also provides insights on the topology of the flow through the analysis of the coherent structures associated with the main modes. In particular, for the liquid sheet flow under study, the DMD provides the spatial distributions of both velocity components (u', v') and volume fraction (C'). Figure 8 reports the real part of the structures corresponding to modes A and B, scaled with respect their maximum. Note that the black dashed line represents the interface location due the mode's action that is computed considering only the correspondent mode in the C reconstruction according to Tu *et al.*[19] and Schmid.[18] Panels (a) and (c) show antisymmetric distributions of u' and C', while panel (b) contains a symmetric distribution of v'. In accordance with Colanera *et al.*,[10] this is typical of a sinuous motion. The v' distribution [panel (b)] along the axis $y/H = 0$ features the same behavior as the 1D leading eigenfunction reported in Fig. 3, namely, an almost monotonic increase in the transverse velocity component along the downstream direction. A similar behavior can be also observed for the mode B, which is a generic mode representative of the flow topology in this branch. Indeed, panels from (d) to (f) report structures with smaller spatial scales with respect the previous

Published under an exclusive license by AIP Publishing

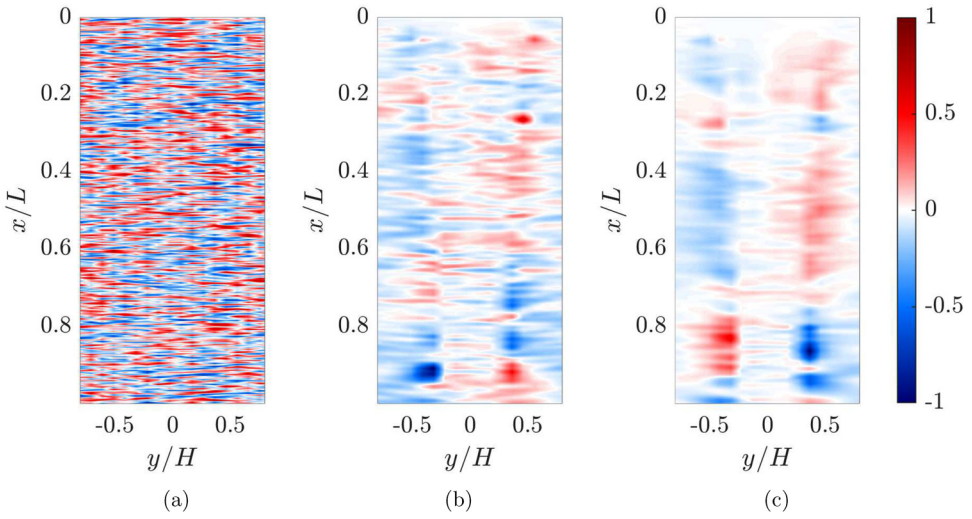

FIG. 6. u' random initial disturbance (a) and its temporal evolution (b) and (c). $We = 2.5$, $Fr = 0.33$, $\varepsilon = 0.02$, $r_\rho = 0.01$, and $Re = 413$. Field variables have been normalized with respect to the maximum.

ones, but still characterized by a sinuous motion. The topology described above is retrieved, with different scales, in all modes of this branch, which is therefore characterized by a purely sinuous behavior. The same characteristics are obtained for the mode F (not reported herein) belonging to the lower branch, whose eigenvalues physically are associated with fast traveling waves with a sinuous behavior. Thus, bearing in mind that the 1D model is purely sinuous, it is not surprising that for these two sinuous branches, there is a good agreement between both spectra.

As will be detailed in the following, the additional 2D middle branch is associated with a varicose flow behavior, which could not be predicted by the 1D model, accounting for the sinuous dynamics only.

To proceed further with the discussion of the spectrum, it is convenient to recall that each mode $\boldsymbol{\varphi}_j$ can be decomposed in sinuous and varicose contributions[10]

$$\boldsymbol{\varphi}_j(x,y) = \boldsymbol{\varphi}_j^s(x,y) + \boldsymbol{\varphi}_j^v(x,y), \tag{25}$$

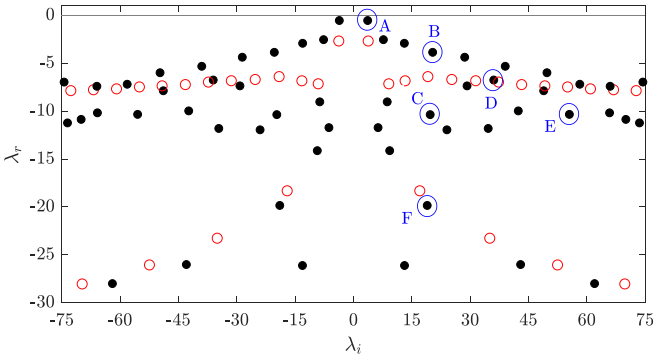

FIG. 7. Data-driven BiGlobal spectrum. $We = 2.5$, $Fr = 0.33$, $\varepsilon = 0.02$, $r_\rho = 0.01$, and $Re = 413$. Black dots refer to the 2D simulations, and red circles represent 1D model results. Letters denote selected modes.

where $\boldsymbol{\varphi}_j^s(x,y)$ and $\boldsymbol{\varphi}_j^v(x,y)$ are the sinuous and varicose components of the mode, respectively. $\boldsymbol{\varphi}_j^s(x,y)$ contains the antisymmetric part (with respect to the axis $y/H = 0$) of u' and C' modes and the symmetric one of v', while $\boldsymbol{\varphi}_j^v(x,y)$ the complementary distributions. Note that sinuous and varicose components are orthogonal to each other by definition. This decomposition can be directly extended to the perturbations energy, E, of Eq. (13). In this way, the energy reads $E = E^s + E^v$, where E^s and E^v represent the sinuous and varicose contributions, respectively. Table IV reports the energy contents for the selected DMD modes.

Looking at the table, one can note that, as expected, the first two modes (A and B) contain a sinuous energy contribution around the 93%; a similar energy distribution can be observed also for the mode F, for which $E^s = 89\%$. Different energy contents are observed in the central branch for increasing frequencies; indeed, modes C, D, and E exhibit a growing varicose energy content, respectively, equal to $E^v = 22.0\%$, 52.1%, and 77.1%.

Bearing in mind the previous energy distributions, Fig. 9 reports the varicose component of the u' modes for eigenvalues C, D, and E. The black dashed line represents the interface location, highlighting the cross-sectional area variation in varicose regime.

TABLE III. Selected eigenvalues of Fig. 7 for the case of $We = 2.5$, $Fr = 0.33$, $\varepsilon = 0.02$, $r_\rho = 0.01$, and $Re = 413$.

	λ_k	
A	−0.54	+3.64 i
B	−3.86	+20.36 i
C	−10.36	+19.73 i
D	−6.75	+36.08 i
E	−10.33	+55.51 i
F	−18.96	+19.84 i

Published under an exclusive license by AIP Publishing

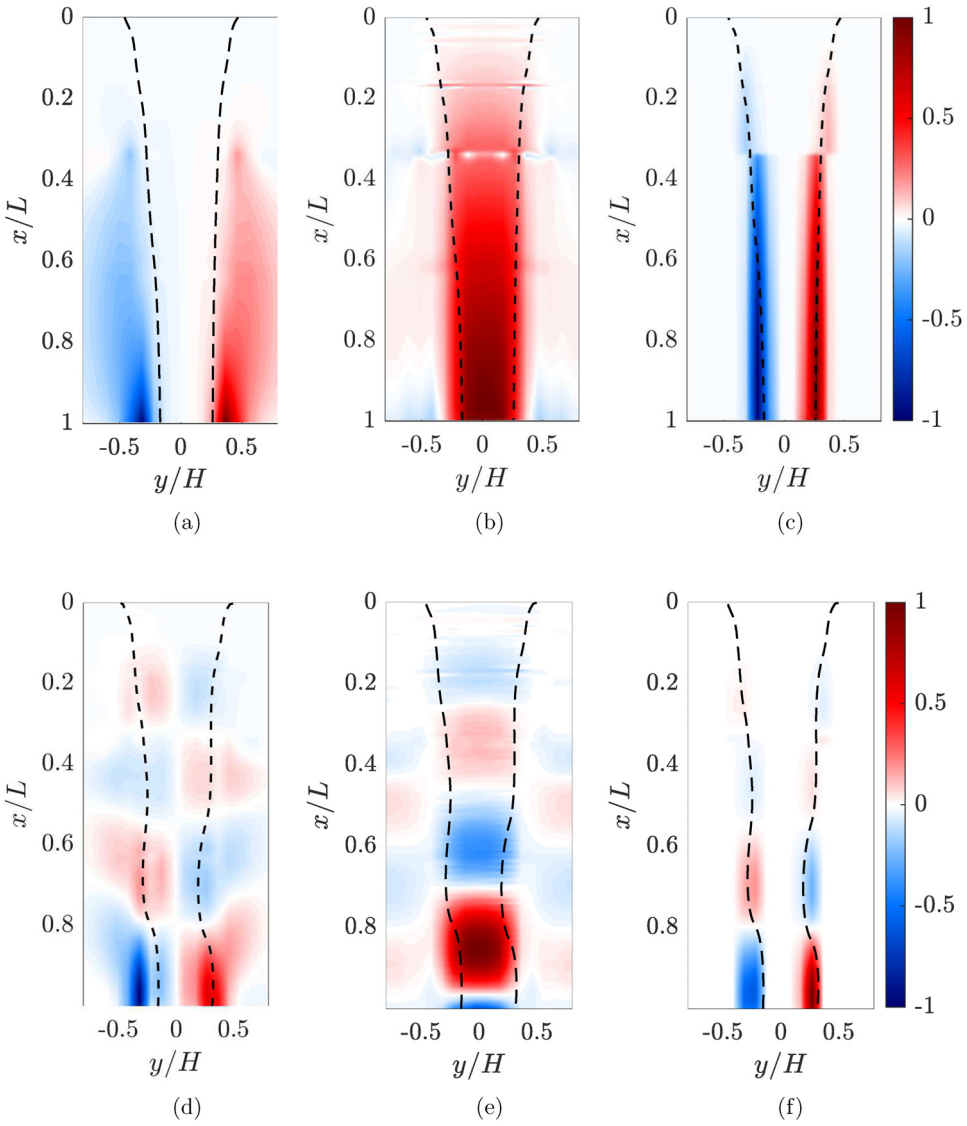

FIG. 8. Spatial distributions of the DMD modes A [panels (a)–(c)] and B [panels (d)–(f)]. $We = 2.5$, $Fr = 0.33$, $\varepsilon = 0.02$, $r_\rho = 0.01$, and $Re = 413$. The black dashed line represents the interface location. Field variables are normalized with respect to the maximum.

TABLE IV. Sinuous and varicose energy contributions of the selected DMD modes. $We = 2.5$, $Fr = 0.33$, $\varepsilon = 0.02$, $r_\rho = 0.01$, and $Re = 413$.

λ_k	E^s(%)	E^v(%)
A	93.5%	6.5%
B	93.5%	6.5%
C	78.0%	22.0%
D	47.9%	52.1%
E	22.9%	77.1%
F	89.0%	11.0%

Moving from C to E, a frequency increase is accompanied by a global decrease in the spatial scales. The resulting wavelength reduction determines a more uniform energy distribution along the sheet length. This can be inferred considering the spatial distributions of the modes' amplitude, which represents the local contribution of the mode to the energy defined in Eq. (13). The corresponding energy distributions are reported in Fig. 10; the energy of the mode C is mainly concentrated downstream of the station $x/L = 0.6$, whereas the modes D and E show a more homogeneous distribution starting from $x/L = 0.5$ and 0.4, respectively.

As discussed also for the 1D case, the convergence and the saturation of the algorithm have been evaluated by means of the analysis

Published under an exclusive license by AIP Publishing

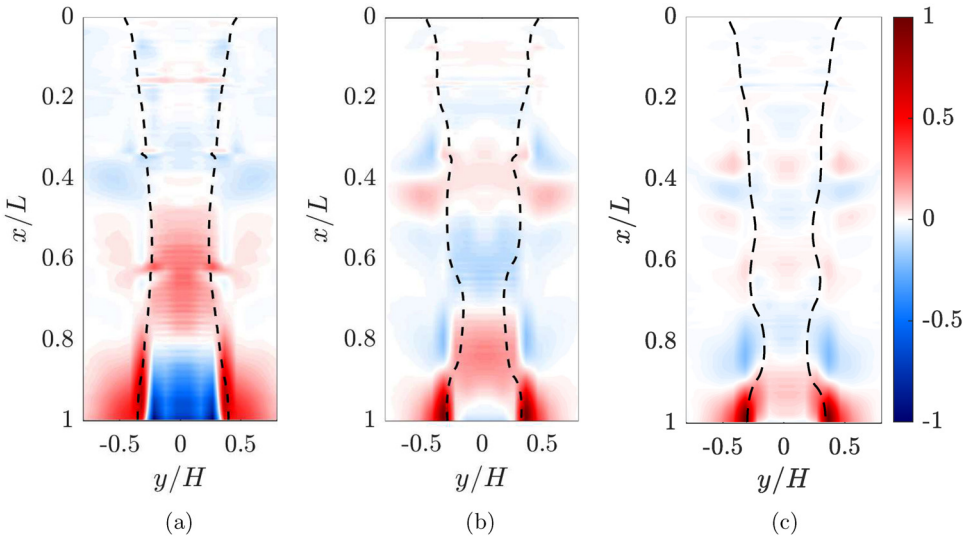

FIG. 9. Varicose component of DMD modes of u' corresponding to eigenvalues C [panel (a)], D [panel (b)], and E [panel (c)]. $We = 2.5$, $Fr = 0.33$, $\varepsilon = 0.02$, $r_\rho = 0.01$, and $Re = 413$. The black dashed line represents the interface location. Field variables are normalized with respect to the maximum.

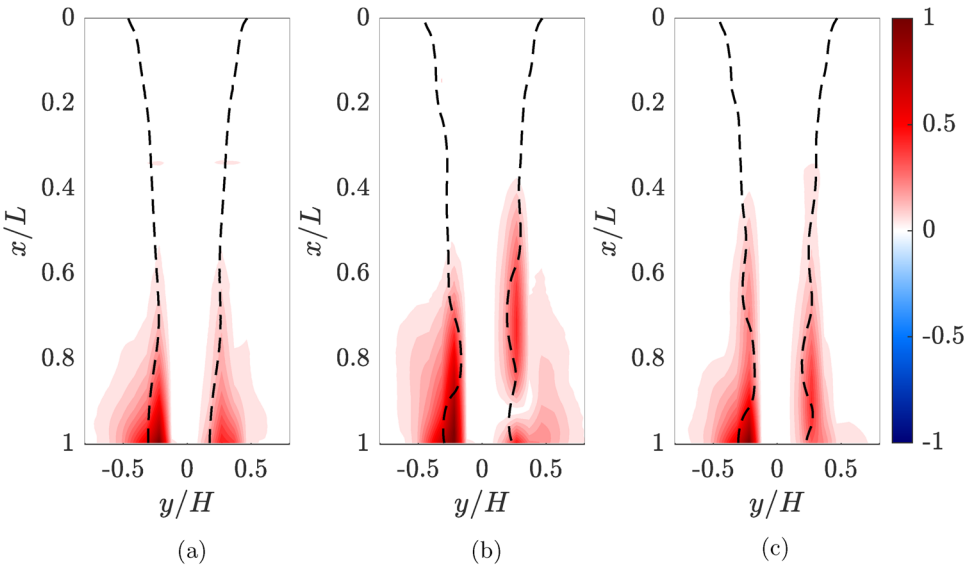

FIG. 10. Energy distribution for the modes C [panel (a)], D [panel (b)], and E [panel (c)]. $We = 2.5$, $Fr = 0.33$, $\varepsilon = 0.02$, $r_\rho = 0.01$, and $Re = 413$. The black dashed line represents the interface location. Field variables are normalized with respect to the maximum.

of the residual **r**. Its trend is reported in Fig. 11, which shows that the residual rapidly tends toward 10^{-13} using about 95 random initializations.

1. Weber number effect

This section investigates how the Weber number affects the eigenspectra and the leading frequencies in both supercritical and subcritical regimes. Changes in the *We* number have been obtained by varying the surface tension (σ), keeping constant the inlet axial velocity U in order to not include effects related to Reynolds and Froude number variations. The analysis has been carried out considering the following reference values: $Fr = 0.33$, $\varepsilon = 0.02$, $r_\rho = 0.01$, and $Re = 413$. Note that in this work only the effects of the Weber number and the density ratio have been considered, as previous works[6–11] have shown that these parameters are the ones with the greatest influence on the behavior of the flow.

The analysis starts considering the flow in supercritical conditions for three different *We* numbers, equal to $We = 1.5$, 2.5, and 3.5. The corresponding dimensionless spectra are reported in Fig. 12,

Published under an exclusive license by AIP Publishing

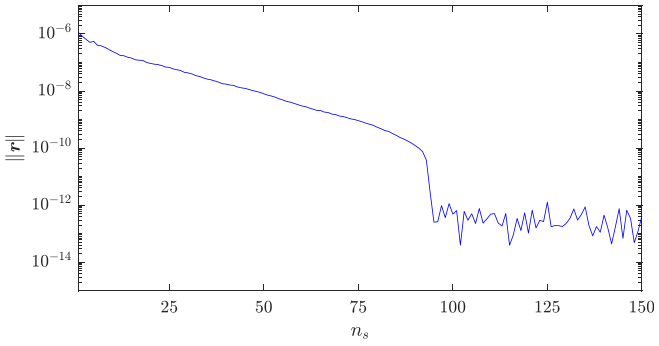

FIG. 11. Convergence of DMD algorithm. Residual history of the DMD vs number of random simulations n_s for the base case ($We = 2.5$, $Fr = 0.33$, $\varepsilon = 0.02$, $r_\rho = 0.01$, and $Re = 413$).

which reveals that, for all these We values, the flow is stable. When We increases, at high frequencies the middle branch moves toward the upper one, and the corresponding modes tend to lose their varicose characteristic assuming a pure sinuous behavior. The leading frequencies are in good agreement with the corresponding ones of the 1D model; the frequency values (λ_i) and the relative spreads (normalized with respect to the 1D model values) are summarized in Table V.

When the Weber number decreases under the unit threshold, the surface tension has a great influence on the flow field, and the behavior of the curtain radically changes. Indeed, passing from supercritical to subcritical conditions, the damping rate increases together with the leading frequency which presents a jump of about an order of magnitude. The experimental evidence of this phenomenon has been recently presented in the work by Chiatto and Della Pia.[40]

Figure 13 contains the dimensionless spectra for $We = 0.75$ (red dots) and $We = 1.5$ (black dots). The leading modes are highlighted with vertical solid lines, and the corresponding frequencies are equal to $\lambda_i = 2.95$ and 16.69 for the supercritical and subcritical case, respectively. For the subcritical spectrum, the second leading eigenvalue is also highlighted (vertical dashed line at $\lambda_i = 31.64$); the first two leading eigenvalues have a similar growth rate, and the spectrum does not reveal the slow branch. Table VI reports the first two leading

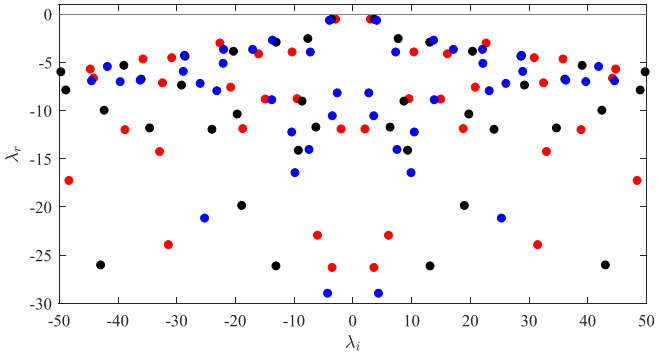

FIG. 12. Effect of the We number on the global spectrum in supercritical regime. Red filled markers represent the DMD spectrum at $We = 1.5$; black ones at $We = 2.5$ and blue ones at $We = 3.5$. $Fr = 0.33$, $\varepsilon = 0.02$, $r_\rho = 0.01$, and $Re = 413$.

TABLE V. Comparison of the leading dimensionless frequency (λ_i) of the DMD and 1D model at various supercritical Weber numbers. The spread refers to the percentage difference between the values normalized with respect to the 1D model one.

	We		
	1.5	2.5	3.5
DMD	2.95	3.64	4.02
1D model	2.99	3.78	4.07
% spread	1.4%	3.7%	1.2%

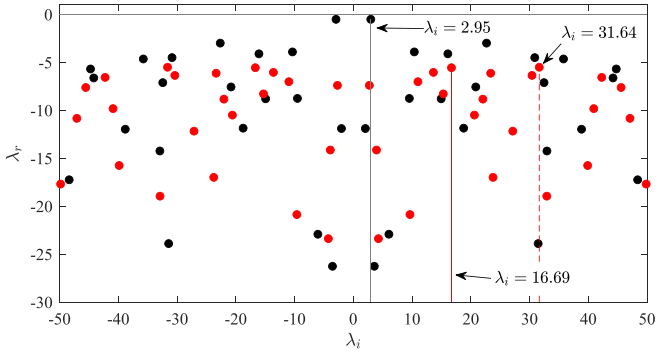

FIG. 13. DMD spectra comparison between supercritical and subcritical regimes. Black filled markers represent the DMD spectrum at $We = 1.5$ and red ones at $We = 0.75$. Vertical solid lines highlight the leading eigenvalues. The red dashed line refers to the second most unstable eigenvalue of the $We = 0.75$ case. $Fr = 0.33$, $\varepsilon = 0.02$, $r_\rho = 0.01$, and $Re = 413$.

eigenvalues together with their sinuous and varicose energy contents. Unlike the previous cases, here the second leading eigenvalue has already a remarkable varicose energy content, about the 53%.

The spatial distributions of the leading DMD mode (with $\lambda_i = 16.69$) highlight a sinuous behavior, similar to those of the supercritical conditions [see panels (a)–(c) of Fig. 8] but with a lower spatial wavelength; therefore, they have not been reported here. The second leading eigenvalue, as already said, presents a relevant amount of energy related to the varicose motion; the corresponding spatial distributions of u' and C' are reported in panels (a) and (b) of Fig. 14. Panel (c) contains both real (black line) and imaginary (red line) parts of the thickness mode φ_h that has been computed as: $\varphi_h = \int_{-1}^{1} \varphi_C \, d\hat{y}$, where $\hat{y} = y/H$.

To give further insights on the behavior of the sheet in the subcritical regime, it is convenient to recover the centerline displacement mode from the spatial distribution of the volume of fluid C' one. In particular, given a C' mode distribution $\varphi_C(x, y)$, the lateral displacement mode $\varphi_\ell(x)$ is calculated as

TABLE VI. Sinuous and varicose energy contents of the first two leading eigenvalues for the case at $We = 0.75$, $Fr = 0.33$, $\varepsilon = 0.02$, $r_\rho = 0.01$, and $Re = 413$.

λ_r	λ_i	$E^s(\%)$	$E^v(\%)$
−5.51	16.69	93.5%	6.5%
−5.56	31.64	46.3%	53.7%

Published under an exclusive license by AIP Publishing

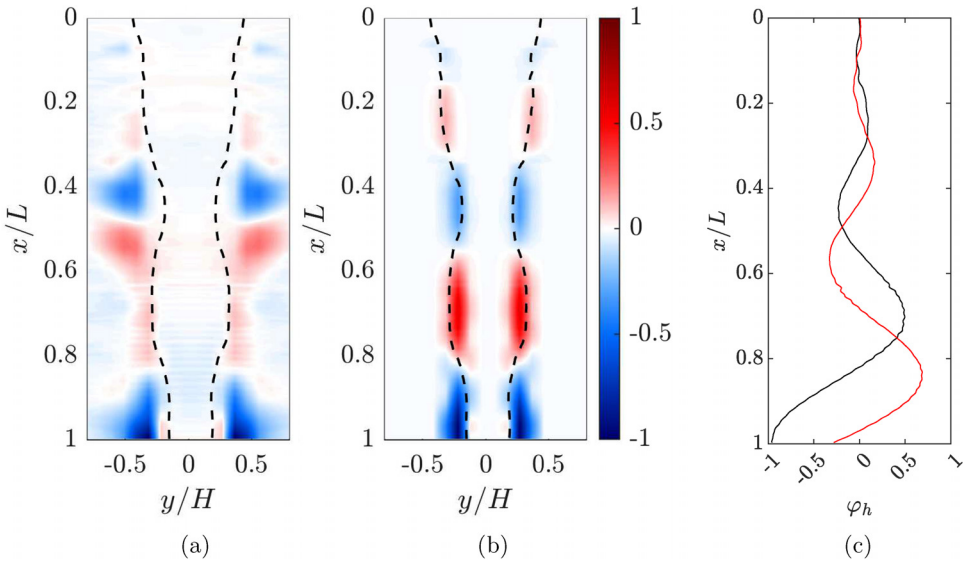

FIG. 14. Varicose components of DMD modes with $\lambda_i = 31.63$ [panels (a) and (b)]. $We = 0.75$, $Fr = 0.33$, $\varepsilon = 0.02$, $r_\rho = 0.01$, and $Re = 413$. The black dashed line represents the interface location. Field variables have been normalized with respect to the maximum. Panel (c) reports the real (black line) and imaginary (red line) parts of the thickness mode.

$$\varphi_\ell(\hat{x}) = \frac{\int_{-1}^{1} \varphi_C \hat{y}\, \mathrm{d}\hat{y}}{\int_{-1}^{1} \bar{C}\, \mathrm{d}\hat{y}}. \tag{26}$$

Panels (a) and (b) of Fig. 15 report real (solid line) and imaginary parts (dash-dotted line) of the leading lateral displacement mode (φ_ℓ) for $We = 0.75$ and $We = 1.5$, respectively.

Apart from the different spatial wavelength, the main difference between these modes is the disturbances traveling time. To clarify this, it is useful to compute the dimensionless phase velocity distributions $c_{ph}(\hat{x}) = \lambda_i/\alpha$ for both modes, where $\alpha(\hat{x})$ is the leading spatial wavelength, depending on the position $\hat{x}$, and it is equal to $\alpha(\hat{x}) = \mathrm{d}\theta/\mathrm{d}\hat{x}$, where the phase distribution is $\theta(\hat{x}) = \arg(\varphi_\ell(\hat{x}))$. The corresponding phase velocities for $We = 0.75$ and 1.5 are reported in the panel (c) in black and red lines, respectively. Considering that the phase velocity of the leading mode at the lower We is always higher than that at the higher We, the crossing time in the subcritical configuration will be smaller. This finding agrees with the results of the 1D model discussed in the previous works of Della Pia *et al.*[6] and Girfoglio *et al.*[4]

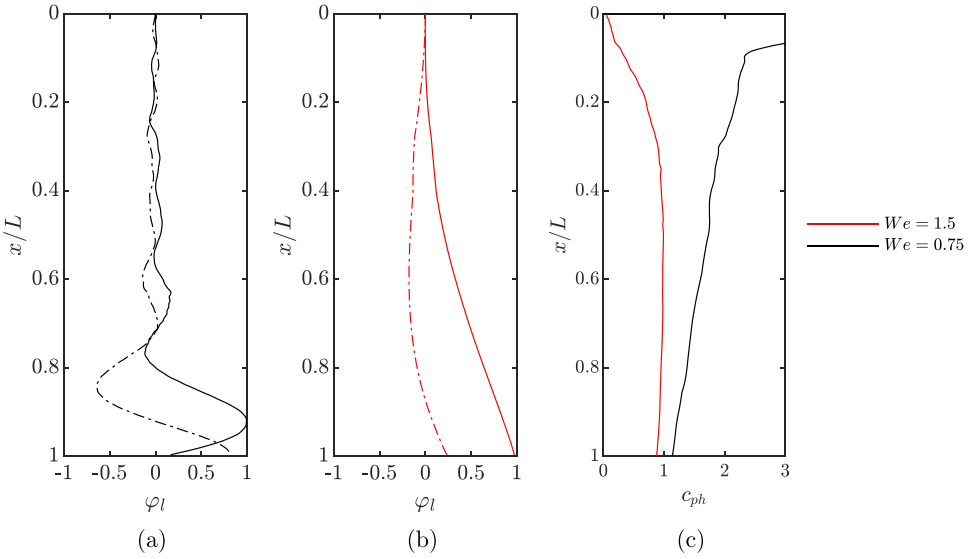

FIG. 15. Leading modes lateral displacement (φ_ℓ) for $We = 0.75$, panel (a), and $We = 1.5$, panel (b). The solid lines are the real parts, and the dash-dotted lines are the imaginary ones. Modes have been normalized with respect to the maximum amplitude. Panel (c) reports the phase velocity c_{ph} of the modes.

Published under an exclusive license by AIP Publishing

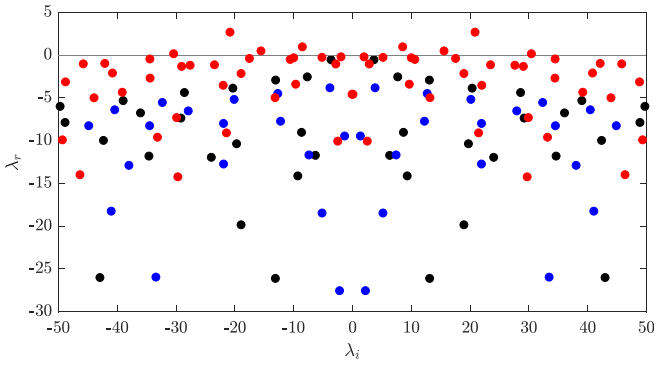

FIG. 16. Density ratio r_ρ effect on DMD spectrum. Red filled markers represent the DMD spectrum at $r_\rho = 0.05$; black ones at $r_\rho = 0.01$, and blue ones at $r_\rho = 0.005$. $We = 2.5$, $Fr = 0.33$, $\varepsilon = 0.02$, and $Re = 413$.

2. Density ratio effect

The density ratio r_ρ has a great impact on the stability of the flow. Here, three different r_ρ values, equal to $r_\rho = 0.005$, 0.01, and 0.05, have been considered, whose spectra are reported in Fig. 16. The analysis has been carried out considering $We = 2.5$. Increasing the density ratio up to $r_\rho = 0.05$, the flow shows an unstable behavior. The most unstable eigenvalue is equal to $\lambda = 2.69 + 20.85i$, with a characteristic frequency in good agreement with that reported in the work by Della Pia *et al.*[6] (Table VI), that regards the frequency response to an impulse disturbance of the transversal velocity component.

A comparison between frequencies of the leading DMD modes and the most unstable eigenvalues of the 1D model is presented in Table VII. A good agreement is retrieved for $r_\rho \leq 0.01$, with a relative spread of about the 5%. For the case $r_\rho = 0.05$, the frequencies of the first two most unstable eigenvalues are reported, because, according to the work by Della Pia *et al.*,[6] a better agreement between VOF simulations and 1D model is found for the imaginary part of the second most unstable eigenvalue ($\lambda_i = 22.60$) rather than the leading one ($\lambda_i = 34.47$). In fact, the ripples of shorter wavelength are likely damped in the more realistic 2D VOF simulations.

The DMD structures for the stable cases at $r_\rho = 0.005$ and 0.01 feature a purely sinuous shape and, being quite similar to those shown in Fig. 8, they are not reported herein. On the contrary, the unstable condition found for $r_\rho = 0.05$ presents leading modes with a different and very interesting spatial distribution. In this last case, the investigation is carried out decomposing the flow field into sinuous and varicose contributions as shown in Eq. (25).

TABLE VII. Effect of the r_ρ on the leading frequency. For the case $r_\rho = 0.05$, the frequencies of the first two most unstable eigenvalues are reported.

	r_ρ		
	0.005	0.01	0.05
DMD	3.85	3.64	20.85
1D model	4.07	3.78	34.47–22.60
% spread	5.4%	3.7%	39.5%–7.7%

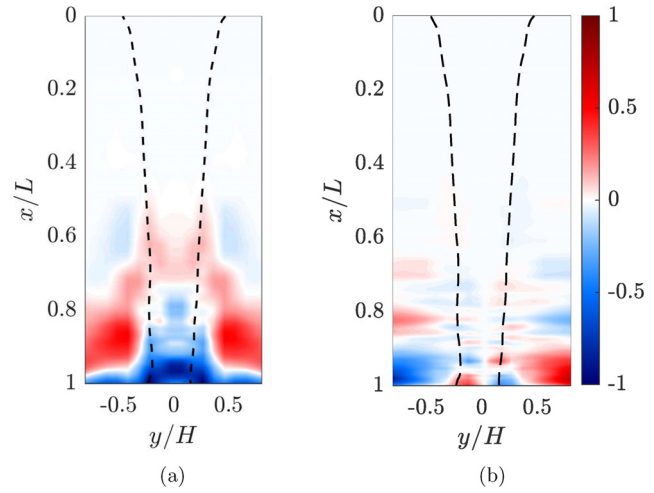

FIG. 17. Varicose components of the DMD leading mode of u' [panel (a)] and v' [panel (b)] for $\lambda_i = 20.85$. $We = 2.5$, $Re = 413$, $Fr = 0.33$, $\varepsilon = 0.02$, and $r_\rho = 0.05$. Field variables are normalized with respect to the maximum.

The energy content of the sinuous and varicose components of the leading mode is equal to $E^s = 57.0\%$ and $E^v = 43.0\%$, respectively. This unstable case is therefore characterized by a relevant varicose content, unlike what has been observed in the previous stable cases, exhibiting a predominant sinuous behavior. Moreover, the amplitude of the varicose components increases downstream, as can be observed by the corresponding spatial distributions reported in Fig. 17.

Further insights on the topology of the leading mode can be obtained by analyzing the local contribution E_x of the sinuous and varicose components to the total energy E of the mode. This contribution is obtained for each mode by integrating the Eq. (13) along the spanwise direction y only, and therefore, E_x depends on the x/L station. Furthermore, as the orthogonality between the sinuous and varicose components is also found locally, one can write $E_x = E_x^s + E_x^v$, where E_x^s and E_x^v are the sinuous and varicose contributions to the total energy, respectively. Figure 18 contains the spatial distribution along

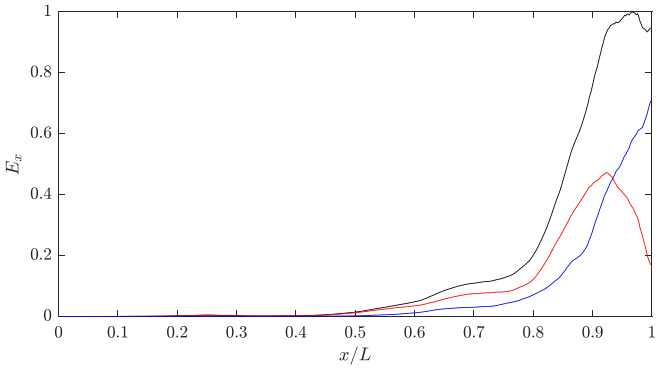

FIG. 18. Spatial distribution of the local norm E_x (black line) together with the corresponding sinuous (red) and varicose (blue) contributions normalized with respect the maximum of E_x. $We = 2.5$, $Re = 413$, $Fr = 0.33$, $\varepsilon = 0.02$, and $r_\rho = 0.05$.

Published under an exclusive license by AIP Publishing

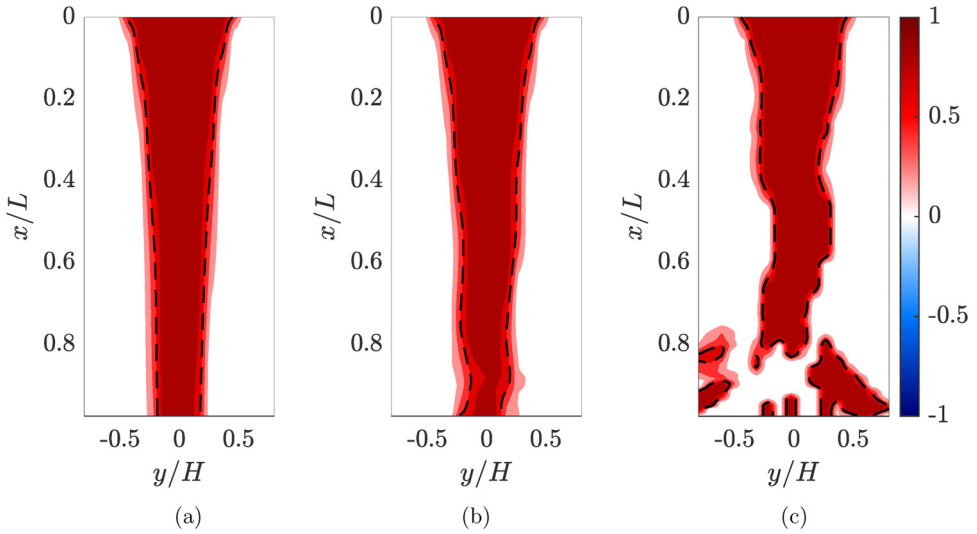

FIG. 19. DMD reconstruction for the C field, considering the leading unstable mode only. Panels from (a) to (c) report its temporal evolution. $We = 2.5$, $Re = 413$, $Fr = 0.33$, $\varepsilon = 0.02$, and $r_\rho = 0.05$.

the longitudinal direction x of the local norm E_x together with E_x^s and E_x^v. Curves have been normalized with respect to the E_x maximum. The inspection of this figure reveals that the rupture mechanism of an unstable liquid jet is deeply related to the amplification of the varicose mode. Indeed, the leading mode is mainly sinuous until $x/L \approx 0.9$, while the varicose behavior gains prominence moving downstream. The shift from sinuous to varicose shape is strictly related to the curtain instability, leading to the rupture of the sheet.

Figure 19 reports the DMD reconstructions of the volume fraction field C at different time instances for this unstable case. By looking at the panel (b), which refers to a time instance before the curtain rupture, it is possible to note that the liquid phase (where $C = 1$, dark red) reports a greater thickness reduction around $x/L = 0.9$ that corresponds to the aforementioned varicose behavior. The sheet rupture can be appreciated in the panel (c).

V. CONCLUSIONS

A data-driven approach, based on the dynamic mode decomposition, has been employed to obtain 2D global (BiGlobal) spectra of gravitational viscous liquid sheet flows in both supercritical and subcritical regimes. The flow fields have been obtained by means of the BASILISK computer code, considering a one-fluid formulation and the volume-of-fluid approach.

The procedure has been verified considering first simplified 1D equations, modeling the lateral displacement and the transversal velocity of the sheet. The estimated eigenmodes and eigenfunctions quickly convergence toward the standard ones of the linear stability theory, computed with the Chebyshev collocation method.

The BiGlobal spectrum for the supercritical case at $We = 2.5$ shows three different branches. The upper and the lower branches, already observed with the 1D model, are associated with the crossing time of slow and fast traveling waves, respectively; they exhibit a purely sinuous behavior with frequencies quite close to those predicted by the 1D model. The middle branch, instead, presents a predominant varicose component, increasing with the frequency, and a uniform energy distribution along the curtain. This last branch could not be predicted by the 1D model, which takes into account the curtain sinuous behavior only.

A parametric investigation has also been performed, to elucidate the impact of the Weber number and the density ratio between the two phases on the dynamics of the curtain. In the supercritical regime, for moderate values of We, the flow is stable and the leading eigenmodes are purely sinuous. When We increases, the varicose middle branch moves toward the upper one at high frequencies. The subcritical regime, instead, shows a leading mode with a frequency almost an order of magnitude higher than the previous ones, but still with a sinuous behavior; the second most unstable eigenvalue has a growth rate comparable with the leading one and a varicose behavior.

In the supercritical regime, increasing the density ratio, flow instabilities arise. The topology of the leading modes reveals how in the unstable configuration there is a superposition of both sinuous and varicose regimes. By means of the inspection of the streamwise contribution to the total energy of the leading mode, some insights on the disturbance propagation have been shown. In particular, moving downstream along the curtain there is a prominent shift from the sinuous shape to the varicose one, highlighting that the instability mechanism, which leads to the rupture of the sheet, is deeply related to the amplification of the varicose modes.

ACKNOWLEDGMENTS

The authors would like to acknowledge Luigi de Luca for inspiring the work.

AUTHOR DECLARATIONS

Conflict of interest

The authors have no conflicts to disclose.

Published under an exclusive license by AIP Publishing

Author Contributions

Antonio Colanera: Investigation (equal); Methodology (equal); Writing – original draft (equal). **Alessandro Della Pia:** Investigation (equal); Methodology (equal); Writing – original draft (equal). **Matteo Chiatto:** Investigation (equal); Methodology (equal); Writing – review & editing (equal).

DATA AVAILABILITY

The data that support the findings of this study are available from the corresponding author upon reasonable request.

REFERENCES

[1]S. Weinstein and K. Ruschak, "Coating flows," Annu. Rev. Fluid Mech. **36**, 29–53 (2004).
[2]L. D. Soderberg, "Absolute and convective instability of a relaxational plane liquid jet," J. Fluid Mech. **493**, 89–119 (2003).
[3]A. M. Binnie, "Resonating waterfalls," Proc. R. Soc. London, Ser. A **339**, 435–449 (1974).
[4]M. Girfoglio, F. De Rosa, G. Coppola, and L. de Luca, "Unsteady critical liquid sheet flows," J. Fluid Mech. **821**, 219–247 (2017).
[5]M. Lodomez, B. Tullis, P. Archambeau, V. Kitsikoudis, M. Pirotton, B. Dewals, and S. Erpicum, "Nappe oscillations on free-overfall structures, data from laboratory experiments," Sci. Data **7**, 180 (2020).
[6]A. Della Pia, M. Chiatto, and L. de Luca, "Global eigenmodes of thin liquid sheets by means of volume-of-fluid simulations," Phys. Fluids **32**, 082112 (2020).
[7]A. Della Pia, A. Colanera, and M. Chiatto, "Surface tension-induced instability in spatially developing subcritical liquid curtains," Phys. Fluids **34**, 042122 (2022).
[8]A. Della Pia, A. Colanera, M. Chiatto, and L. de Luca, "Energy insights into the unsteady dynamics of a viscous gravitational liquid sheet," Phys. Fluids **33**, 092118 (2021).
[9]A. Arote, M. Bade, and J. Banerjee, "On coherent structures of spatially oscillating planar liquid jet developing in a quiescent atmosphere," Phys. Fluids **32**, 082111 (2020).
[10]A. Colanera, A. Della Pia, M. Chiatto, L. de Luca, and F. Grasso, "Modal decomposition analysis of unsteady viscous liquid sheet flows," Phys. Fluids **33**, 092117 (2021).
[11]A. Della Pia, M. Chiatto, and L. de Luca, "Receptivity to forcing disturbances in subcritical liquid sheet flows," Phys. Fluids **33**, 032113 (2021).
[12]S. Schmidt and K. Oberleithner, "Instability of forced planar liquid jets: Mean field analysis and nonlinear simulation," J. Fluid Mech. **883**, A7 (2020).
[13]K. Taira, M. S. Hemati, S. L. Brunton, Y. Sun, K. Duraisamy, S. Bagheri, S. T. M. Dawson, and C. Yeh, "Modal analysis of fluid flows: Applications and outlook," AIAA J. **58**, 998–1022 (2020).
[14]C. Hou, N. Deng, and B. R. Noack, "Trajectory-optimized cluster-based network model for the sphere wake," Phys. Fluids **34**, 085110 (2022).
[15]Z. Ma, J. Yu, and R. Xiao, "Data-driven reduced order modeling for parametrized time-dependent flow problems," Phys. Fluids **34**, 075109 (2022).
[16]I. Mezic, "Spectral properties of dynamical systems, model reduction and decompositions," Nonlinear Dyn. **41**, 309–325 (2005).
[17]C. Rowley, I. Mezi, S. Bagheri, P. Schlatter, and D. Henningson, "Spectral analysis of nonlinear flows," J. Fluid Mech. **641**, 115–127 (2009).
[18]P. J. Schmid, "Dynamic mode decomposition of numerical and experimental data," J. Fluid Mech. **656**, 5–28 (2010).
[19]J. Tu, C. Rowley, D. Luchtenburg, S. Brunton, and J. Kutz, "On dynamic mode decomposition: Theory and applications," J. Comput. Dyn. **1**, 391–421 (2013).
[20]P. Schmid, "Dynamic mode decomposition and its variants," Annu. Rev. Fluid Mech. **54**, 225–254 (2022).
[21]S. Tirunagari, N. Poh, D. Windridge, A. Iorliam, N. Suki, and A. T. S. Ho, "Detection of face spoofing using visual dynamics," IEEE Trans. Inf. Forensics Security **10**, 762–777 (2015).
[22]B. Brunton, L. Johnson, J. Ojemann, and J. Kutz, "Extracting spatial-temporal coherent patterns in large-scale neural recordings using dynamic mode decomposition," J. Neurosci. Methods **258**, 1–15 (2016).
[23]P. G. Drazin and W. H. Reid, *Hydrodynamic Stability*, 2nd ed., Cambridge Mathematical Library (Cambridge University Press, 2004).
[24]P. Schmid and D. Henningson, *Stability and Transition in Shear Flows*, Applied Mathematical Sciences (Springer, New York, 2012).
[25]W. O. Criminale, T. L. Jackson, and R. D. Joslin, "Theory and computation of hydrodynamic stability," *Cambridge Monographs on Mechanics* (Cambridge University Press, 2003).
[26]X. Chen, J. Lu, S. Zaleski, and G. Tryggvason, "Characterizing interface topology in multiphase flows using skeletons," Phys. Fluids **34**, 093312 (2022).
[27]E. Ferrer, J. de Vicente, and E. Valero, "Low cost 3D global instability analysis and flow sensitivity based on dynamic mode decomposition and high-order numerical tools," Int. J. Numer. Methods Fluids **76**, 169–184 (2014).
[28]R. Ranjan, S. Unnikrishnan, and D. Gaitonde, "A robust approach for stability analysis of complex flows using high-order Navier-Stokes solvers," J. Comput. Phys. **403**, 109076 (2020).
[29]B. Herrmann, P. J. Baddoo, R. Semaan, S. L. Brunton, and B. J. McKeon, "Data-driven resolvent analysis," J. Fluid Mech. **918**, A10 (2021).
[30]J. Kern, M. Beneitez, A. Hanifi, and D. Henningson, "Transient linear stability of pulsating poiseuille flow using optimally time-dependent modes," J. Fluid Mech. **927**, A6 (2021).
[31]S. Popinet, "An accurate adaptive solver for surface-tension-driven interfacial flows," J. Comput. Phys. **228**, 5838–5866 (2009).
[32]R. Scardovelli and S. Zaleski, "Direct numerical simulation of free-surface and interfacial flow," Annu. Rev. Fluid Mech. **31**, 567–603 (1999).
[33]C. W. Hirt and B. D. Nichols, "Volume of fluid (VOF) method for the dynamics of free boundaries," J. Comput. Phys. **39**, 201–225 (1981).
[34]V. Theofilis, *Globally Unstable Basic Flows in Open Cavities* (American Institute of Aeronautics and Astronautics Inc., 2000).
[35]S. Bagheri, E. Akervik, L. Brandt, and D. Henningson, "Matrix-free methods for the stability and control of boundary layers," AIAA J. **47**, 1057–1068 (2009).
[36]F. Gomez, R. Gomez, and V. Theofilis, "On three-dimensional global linear instability analysis of flows with standard aerodynamics codes," Aerosp. Sci. Technol. **32**, 223–234 (2014).
[37]B. T. Chu, "On the energy transfer to small disturbances in fluid flow (Part I)," Acta Mech. **1**, 215–234 (1965).
[38]A. Kornecki, E. Dowell, and J. O'Brien, "On the aeroelastic instability of two-dimensional panels in uniform incompressible flow," J. Sound Vib. **47**, 163–178 (1976).
[39]P. J. Olsson and D. S. Henningson, "Optimal disturbance growth in watertable flow," Stud. Appl. Math. **94**, 183–210 (1995).
[40]M. Chiatto and A. Della Pia, "Natural frequency discontinuity of vertical liquid sheet flows at transcritical threshold," J. Fluid Mech. **945**, A32 (2022).

Published under an exclusive license by AIP Publishing